

## ASTEROSEISMOLOGICAL MODELING OF THE MULTIPERIODIC $\lambda$ BOOTIS STAR 29 CYGNI

R. CASAS, A. MOYA, J. C. SUÁREZ<sup>1</sup>, S. MARTÍN-RUIZ, P. J. AMADO, C. RODRÍGUEZ-LÓPEZ<sup>2</sup>, AND R. GARRIDO  
Instituto de Astrofísica de Andalucía (CSIC), Granada, Spain, CP3004

Received 2008 September 3; accepted 2009 February 26; published 2009 May 4

### ABSTRACT

The present work focuses on the discussion of the  $\lambda$  Bootis nature of the multiperiodic  $\delta$  Scuti star HD 192640 (29 Cyg), through a comprehensive asteroseismic modeling. Some of the most recent asteroseismic tools are used to check whether the observed low metallicity is internal, i.e., intrinsic, present throughout the star, or due to superficial processes as accretion, diffusive settling, radiative levitation, mass loss, etc. The modeling method uses some of the most recent tools, including: (1) effects of rotation on equilibrium models, on the adiabatic oscillation spectrum, and its influence in multicolor observables, (2) nonadiabatic stability of radial and nonradial modes, (3) inclusion of the atmosphere–pulsation interaction for a more accurate multicolor mode identification, and (4) ratio between radial modes  $n = 4$  and  $n = 5$  in the framework of Petersen diagrams. The analysis performed reveals that the models fulfilling all the constraints are those in the middle of the main sequence (MS), with subsolar metallicity, except some other unlikely possibilities. Therefore, this study does not support the idea of the  $\lambda$  Bootis stars being zero-age MS or pre-MS stars interacting with their primordial cloud of gas and dust, but suggest the explanation of their nature as submetallic MS objects. Nevertheless, more accurate multicolor photometric observations are required for a more conclusive study using the procedure presented here, since the observational errors are too large for a definitive rejection of any of the possible explanations.

*Key words:* stars: fundamental parameters – stars: individual (29 Cygni) – stars: oscillations – stars: rotation – stars: variables: other

### 1. INTRODUCTION

Discovered by Morgan et al. (1943), the  $\lambda$  Bootis-type stars are nonmagnetic, moderately rotating, Pop. I stars with spectral types from late B–early A to F (dwarfs),<sup>3</sup> which show peculiarities in the morphology and abundance of the Fe-peak element lines. In particular, these lines are unusually weak considering their spectral types. Significant deficiencies in their abundances (up to 2 dex) are found, whereas C, N, O, and S have solar abundance (Paunzen et al. 2002). To date, different theories have tried to explain the  $\lambda$  Bootis nature from both observational (photometry, spectroscopy) and theoretical investigations. It is not our aim to discuss all these theories here (see Paunzen 2003 for an interesting review). Nevertheless, it may be worth describing the most probable scenarios which rely on the accretion of interstellar medium gas by the star (Venn & Lambert 1990) or mass loss together with diffusive processes (Michaud & Charland 1986). The second possibility was discarded when the meridional circulation was included in the models (Charbonneau 1993), and only the first one remains. The accretion/diffusion scenario would explain the abundances found at the base of the outer convective zone of these stars, since convective layers are assumed to remain chemically homogeneous. The accretion rate required to maintain this situation is of the order of  $10^{-10}$ – $10^{-14} M_{\odot}$  per year (Turcotte & Charbonneau 1993) and, once the accretion has ceased, the metal deficiencies should disappear in 1 Myr approximately due to diffusion and internal mixing processes. Thus, a possible interpretation is that  $\lambda$  Bootis stars are very early A-type stars (in a pre-main sequence (pre-MS) or zero-age MS (ZAMS) evolutionary stage), still interacting with their primordial clouds

of gas and dust. Interestingly, Paunzen et al. (2002) found that most of the known  $\lambda$  Bootis stars lie between the ZAMS and the TAMS (terminal-age MS). In this case the most likely scenario would be an MS star passing through an interstellar cloud (Kamp & Paunzen 2002). Even so, the chemical mixing due to internal processes, such as rotationally induced mixing, cannot yet be discarded as a possible explanation itself of the observed abundances.

Nowadays the  $\lambda$  Bootis stars and other types of stars in the same region of the H-R diagram, such as  $\delta$  Scuti stars, are considered as particularly suitable for the asteroseismological study of poorly known hydrodynamical processes occurring in stellar interiors, like the extent of the convective core, mixing of chemical elements, redistribution of angular momentum (Zahn 1992), etc.  $\lambda$  Bootis-type stars are also pulsating stars. Therefore, asteroseismology can be used to obtain information about the internal structure of these objects. Several works have been devoted to these studies, for instance Paunzen (1998).

The  $\lambda$  Bootis star 29 Cyg (HD 192640, HR 7736) (at  $\alpha = 20^{\text{h}}14^{\text{m}}32^{\text{s}}.0$ ,  $\delta = 36^{\circ}48'.4$ ) was the first  $\lambda$  Bootis star classified as a pulsating variable (Gies & Percy 1977). It is a multiperiodic, small-amplitude ( $\Delta V \sim 0^{\text{m}}.02$ ), pulsating star (Rodríguez et al. 2000). Winzer (1974) searched for variations of the order of days, but no evidence of such variations was found. Gies & Percy (1977) discovered its short-term photometric variations with an estimated period of  $\approx 45$  minutes, with an oscillation amplitude in the V band of the order of 0.02 mag. Handler & Paunzen (1995) confirmed that variability, and established a new dominant period of approximately 39 minutes. Further frequency analyses were performed by Kusakin & Mkrtchian (1996) and Paunzen & Handler (1996). While the former found seven oscillation frequencies, the latter obtained results consistent with the work of Gies & Percy (1977). Rolland et al. (2002) found 14 significant frequencies in a multisite campaign using the 90 cm telescope at Sierra Nevada Observatory

<sup>1</sup> Associated researcher: Observatoire de Paris, LESIA, UMR 8109, Meudon, France.

<sup>2</sup> Current address: Toulouse, France

<sup>3</sup> 2% of the A-type stars belong to this class (Gray & Corbally 2002)

(Granada, Spain) together with the 1.5 m telescope at San Pedro Mártir Observatory (Mexico). In both observatories, twin four-channel simultaneous Strömgen photometers were used. Mkrtichian et al. (2007) presented results of a multisite campaign and a tentative mode identification of this star. The frequencies provided in this reference are almost coincident with those used in our work (taken from Rolland et al. 2002; Table 1).

The present work aims at a comprehensive asteroseismic modeling of 29 Cyg focusing on the discussion of the  $\lambda$  Bootis nature of the star. That is, its aim is to answer whether the observed metallicity is intrinsic to the star or an effect of superficial processes such as accretion together with internal chemical transport (rotationally induced mixing, gravitational settling, radiative levitation, etc). To do so, some of the most updated tools adapted for this purpose are used: (1) the evolutionary code CESAM (Morel 1997), and (2) the pulsation codes GraCo (Moya et al. 2004) and FILOU (Tran Minh & Léon 1995; Suárez 2002). GraCo provides nonadiabatic quantities related to pulsation and includes the atmosphere–pulsation interaction described in Dupret et al. (2002). FILOU includes the effects of rotation on adiabatic oscillations up to the second order in a perturbative theory. Using these tools we performed a massive numerical study of 29 Cyg in an attempt to constrain physical and theoretical parameters. In this work we will follow the same scheme used for the study of RV Arietis (Casas et al. 2006), i.e., the analysis of:

1. the effects of rotation on both the oscillation frequencies and the equilibrium models;
2. the effect in the results of changing the mixing length parameter  $\alpha_{\text{MLT}}$ ;
3. the use of multicolor photometry for mode identification. To do this, calculation of nonadiabatic observables is needed;
4. the pulsational instability of this star.

The two main approximations taken in the models with a possible influence in this study are the neglect of updated internal chemical transport mechanisms in the equilibrium models, such as rotational-induced mixing or gravitational waves, and the use of the “frozen convection approximation” in the pulsational resolution. We are working to add these mechanisms and remove the frozen convection approximation in our models.

The paper is structured as follows: equilibrium models, oscillation computations, and the fundamental parameters of 29 Cyg are described in Section 2. Then, a nonadiabatic analysis is performed in Section 3, including studies of mode-instability ranges. Section 4 focuses on the problem of mode identification, which is undertaken by considering amplitude/phase diagrams in the framework of multicolor photometry, and examining the variation of color indices as a function of the star’s position in the H-R diagram and the stellar rotation. In Section 5, some additional procedures are presented, as the analysis of the evolution of multicolor indices or of a few radial-mode frequency ratios. Finally, conclusions are reported in Section 6.

## 2. PHYSICAL PARAMETERS AND STELLAR SEISMIC MODELS

### 2.1. Physical Parameters

The physical parameters of 29 Cyg ( $\log T_{\text{eff}} = 3.902 \pm 0.009$ ,  $\log g = 4.12 \pm 0.25$ , and  $v \sin i \lesssim 80 \text{ km s}^{-1}$ ) were kindly provided by E. Rodríguez, who derived them

from multicolor photometry (details in Rodríguez et al. 2000 and references therein). These values are compatible with the physical parameters found for this star in the literature (Mkrtichian et al. 2007; Heiter et al. 2002). The star 29 Cyg can be classified as a moderately rotating  $\delta$  Scuti star with  $v \sin i \sim 80 \text{ km s}^{-1}$  (Heiter et al. 2002). Michel et al. (1999) proposed a method of determining the effects of rotation and geometry (angle of inclination of the star) on photometric parameters. In the framework of  $\delta$  Scuti stars that method was then further developed by Pérez Hernández et al. (1999), showing that uncertainties of around 100–150 K in effective temperature, and  $\sim 0.10$  dex in  $\log g$ , can be found for moderately rotating stars. That result was later confirmed by Suárez et al. (2002). In the present case, considering the absence of additional information on the inclination angle of the star, an uncertainty H-R diagram box of  $\sim 150 \text{ K}$  in  $T_{\text{eff}}$  and  $\sim 0.25$  dex in  $\log g$ , is adopted here (see Figure 1).

### 2.2. Stellar Equilibrium Models

The stellar equilibrium models were computed with the evolutionary code CESAM (Morel 1997), using a mesh grid (B-splines basis) of 2000 points. First-order effects of rotation on the equilibrium models were considered by subtracting the spherically averaged contribution of the centrifugal acceleration to the gravity of the model,  $g_{\text{eff}} = g - \mathcal{A}_c(r)$ , where  $g$  corresponds to the local gravity, and  $\mathcal{A}_c(r)$  represents the radial component of the centrifugal acceleration. This spherically averaged component of the centrifugal acceleration does not change the order of the hydrostatic equilibrium equations. Such models are called “pseudo-rotating” models (see Soufi et al. 1998; Suárez et al. 2006). During evolution, models are assumed to rotate as a rigid body, and their total angular momentum is conserved. Although the nonspherical components of the centrifugal acceleration were not considered, they were included as a perturbation in the oscillation computation.

Standard physical inputs for  $\delta$  Scuti stars are used, i.e., the CEFF equation of state (Christensen-Dalsgaard & Daeppen 1992). The opacity tables were taken from the OPAL package (Iglesias & Rogers 1996), complemented at low temperatures ( $T \lesssim 10^4 \text{ K}$ ) by the tables provided by Alexander & Ferguson (1994). The atmosphere was calculated with two approaches: a gray atmosphere (Eddington  $T(\tau)$  law) when the equilibrium models were used to compute adiabatic oscillations, and the Kurucz model atmospheres for the computation of nonadiabatic quantities. The abundance mixture used is that given in Grevesse & Noels (1993).

The left (right) panel of Figure 1 plots evolutionary tracks obtained by covering the four corners and the center of the photometric error box. The  $\lambda$  Bootis stars are classified as Pop. I stars, since the most likely scenario to explain the abundances anomalies in some elements are some physical processes (see Section 1) and not intrusive abundances. Therefore we have studied models with a metallicity  $[M/H] = -0.44$  ( $[M/H] = 0$ ), to explore the most likely range of metallicities for Pop. I stars. The helium mass fractions used are, then,  $Y=0.25$  and  $0.273$ , respectively. Both sets of models are used to check whether the observed metallicity of 29 Cyg is internal or superficial. The rotational velocity used is described in Section 4.1.

### 2.3. Oscillation Computation

The seismic models were completed by computing for each model its corresponding oscillation spectrum.

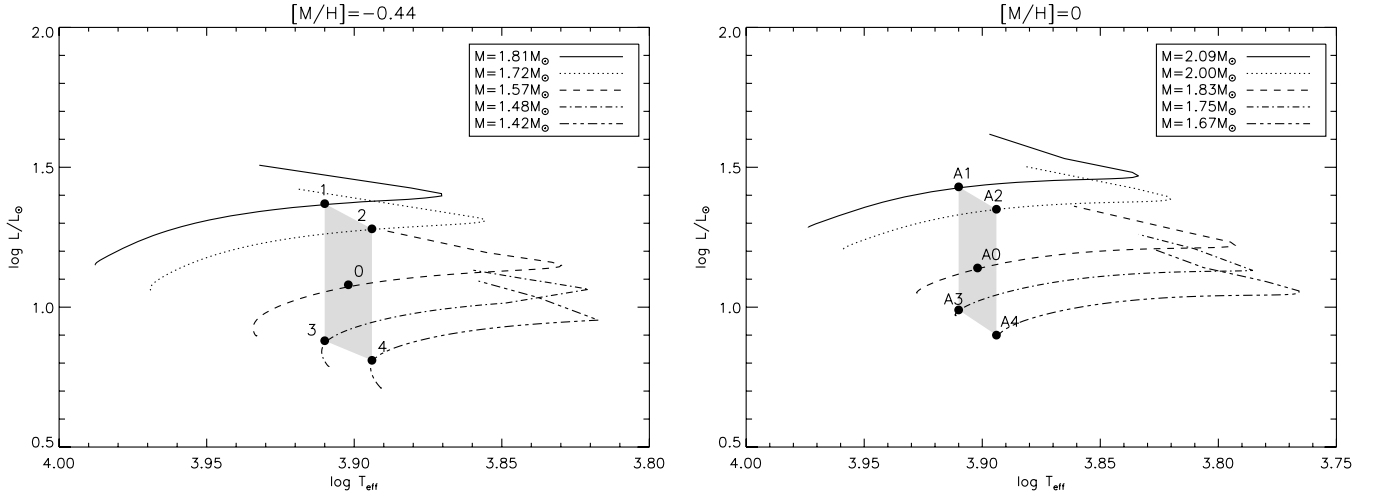


**Figure 1.** H-R diagrams showing the observational photometric error box (shaded surface) for 29 Cyg. Filled circles correspond to models representative of the star, labeled from 0 to 4, covering the extreme regions of the error box (more details in the text). In the left panel, evolutionary tracks for  $[M/H] = -0.44$ , and in the right panel, those with solar metallicity.

**Table 1**

Observed Mean Periods of the Detected Oscillation Frequencies with their Corresponding Mean Amplitudes (Taken from Rolland et al. 2002)<sup>a</sup>

Frequency	P(d)	$\nu$ (c/d)	$\nu$ ( $\mu$ Hz)	$A_v$ (mag)	$f_1/f_{i=2...14}$
$f_1$	0.0336	29.7760	344.63	0.0039	...
$f_2$	0.0288	34.7104	401.74	0.0056	0.858
$f_3$	0.0267	37.4259	433.17	0.0127	0.7956
$f_4$	0.0397	25.1913	291.57	0.0035	1.182
$f_5$	0.0364	27.5067	318.37	0.0032	1.083
$f_6$	0.0393	25.4631	294.71	0.0021	1.169
$f_7$	0.0316	31.6514	366.34	0.0021	0.941
$f_8$	0.0301	33.2451	384.78	0.0020	0.896
$f_9$	0.0304	32.9112	380.92	0.0017	0.905
$f_{10}$	0.0368	27.1457	314.19	0.0014	1.097
$f_{11}$	0.0492	20.3431	335.45	0.0014	1.464
$f_{12}$	0.0317	31.5841	365.56	0.0013	0.943
$f_{13}$	0.0359	27.8326	322.14	0.0012	1.070
$f_{14}$	0.0279	35.8477	414.90	0.0011	0.831

**Note.** <sup>a</sup> Last column gives the frequency ratio  $f_1/f_{i=2...14}$ .

GraCo was used to study the mode instability and estimate the nonadiabatic observables required for multicolor photometric analysis. For such computations, Kurucz atmospheres (Section 2.2) were reconstructed at specific Rosseland optical depths ( $\tau_{\text{Ross}} = 1$ ) until the last photospheric edge of the star was reached.

FILOU was utilized in order to calculate adiabatic oscillations corrected for the effect of rotation up to second order (centrifugal and Coriolis forces), including near-degeneracy effects and the mode contamination coefficients (Suárez et al. 2006), necessary to correct the amplitude ratio/phase difference diagnostic diagrams for the effect of rotation. The  $\nu \sin i$  of 29 Cyg is close to the limit of validity of such second-order perturbation technique, so results should be regarded with caution.

### 3. INSTABILITY ANALYSIS

The first constraint to the modeling considered in our study is given by the instability analysis of the observed frequencies. That is, only the models that predict the instability of observed frequencies are kept. This analysis was performed using

**Table 2**

Main Characteristics of Computed Models Representative of 29 Cyg<sup>a</sup>

ID ( $ij$ )	$M/M_{\odot}$	$T_{\text{eff}}$	$g$	$X_c$	Age	$\alpha_{\text{MLT}}$	$\nu_{\text{min}}$	$\nu_{\text{max}}$	$\Delta z/H_p$	$\nu_f$
00	1.57	3.902	4.12	0.359	1284	1.5	188	661	0.84	186.22
01	1.57	3.902	4.12	0.361	1284	1.0	158	685	0.82	186.10
02	1.57	3.902	4.12	0.360	1282	0.5	148	727	0.74	186.52
10	1.81	3.910	3.92	0.198	1045	1.5	153	456	0.86	126.42
11	1.81	3.910	3.92	0.198	1045	1.0	146	460	0.85	126.43
12	1.81	3.910	3.92	0.198	1045	0.5	135	465	0.76	126.43
20	1.72	3.894	3.92	0.195	1213	1.5	134	439	0.80	129.03
21	1.72	3.894	3.92	0.195	1213	1.0	129	448	0.78	129.03
22	1.72	3.894	3.92	0.195	1213	0.5	129	448	0.70	129.03
30	1.48	3.910	4.32	0.588	772	1.5	249	988	0.85	268.15
31	1.48	3.910	4.32	0.588	772	1.0	246	1030	0.84	268.15
32	1.48	3.910	4.32	0.588	772	0.5	170	1092	0.78	268.15
40	1.42	3.894	4.31	0.575	935	1.5	198	831	0.83	265.27
41	1.42	3.894	4.31	0.575	935	1.0	198	870	0.82	265.28
42	1.42	3.894	4.31	0.575	938	0.5	198	947	0.78	265.08
A02	1.83	3.902	4.12	0.483	670	0.5	204	759	0.78	177.72
A12	2.09	3.910	3.92	0.313	700	0.5	130	473	0.78	121.42
A22	2.00	3.894	3.92	0.303	807	0.5	159	489	0.77	121.32
A32	1.75	3.910	4.29	0.660	170	0.5	211	1050	0.83	238.29
A42	1.67	3.894	4.30	0.680	100	0.5	192	935	0.81	244.91

**Note.** <sup>a</sup> Label  $i$  from 0 to 4 indicates the location of the models in the H-R diagram displayed in Figure 1 with  $[M/H] = -0.44$ , while  $j$  accounts for the  $\alpha_{\text{MLT}}$  used. From left to right,  $M$  represents the stellar mass in solar masses  $M_{\odot}$ ;  $T_{\text{eff}}$  the effective temperature in K (on a logarithmic scale);  $g$  the surface gravity in cgs (on a logarithmic scale);  $X_c$  the central hydrogen mass fraction; the age in Myr;  $\alpha_{\text{MLT}}$  the mixing-length parameter;  $\nu_{\text{min}}$  and  $\nu_{\text{max}}$  represent the frequency range of predicted unstable modes (in  $\mu$ Hz);  $\Delta z/H_p$  the size of the external convective zone normalized by the local pressure scale height, and finally,  $\nu_f$ , the fundamental radial mode (in  $\mu$ Hz). Models labeled as  $Ai2$  have been calculated with solar metallicity and  $\alpha_{\text{MLT}} = 0.5$ .

nonrotating models computed in the manner described in Section 2.3. For the two selected metallicity values, only the models at the center and at the four corners of the photometric error box shown in Figure 1 were considered (Table 2). This selection guarantees a good coverage of the general properties of the models within the photometric uncertainties and avoids redundant computations. Models are identified (ID) with labels

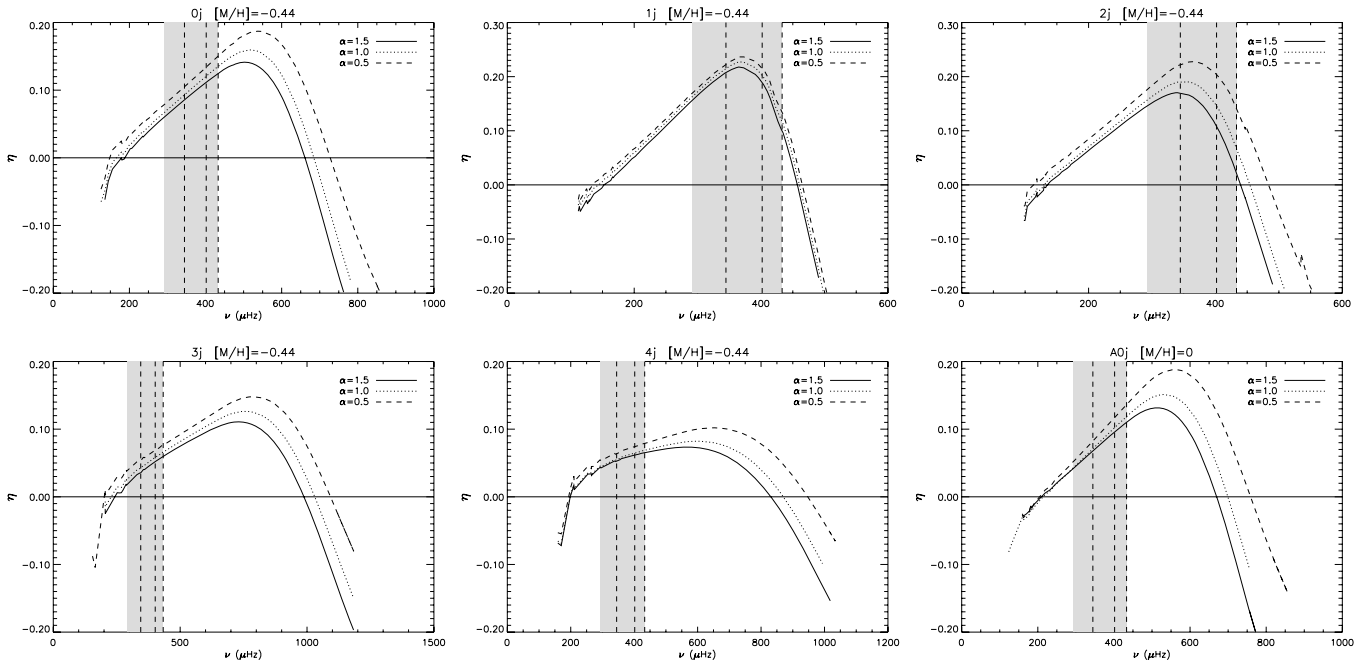


**Figure 2.** Predicted growth rates  $\eta$  for modes in the range of the observed frequencies, as a function of the frequency in  $\mu\text{Hz}$ . Different lines correspond to different values of the mixing-length parameter  $\alpha_{\text{MLT}}$ . Vertical dashed lines represent the observed frequencies  $f_1$ ,  $f_2$ , and  $f_3$ . The shaded area represents the complete frequency range of observed frequencies.

$ij$  with  $i = 0, \dots, 4$  and  $j = 0, 1, 2$ . Label  $i$  indicates the location in the H-R diagram ( $0j$  correspond to central models represented in Figure 1). Label  $j$  indicates a different value of  $\alpha_{\text{MLT}}$  used. The extra set of solar metallicity models are labeled with an  $A$  ( $Aij$ ).

Predictions on the modes' instability are obtained by analyzing the growth rate  $\eta$  in the range of the observed frequencies. When  $\eta > 0$ , modes are predicted to be overstable. The instability ranges found for the whole set of selected models are listed in Table 2. Although most of the selected models predict the observed frequency range to be unstable, significant differences are found in the size of the predicted ranges. In general, the larger the mass of the model and/or the  $\alpha_{\text{MLT}}$  parameter, the lower the total number of unstable modes. Moreover, the lower limit of the instability ranges is nearly independent of the  $\alpha_{\text{MLT}}$  value. This is illustrated in Figure 2 in which the instability range predicted by the models is compared with the range of the observed frequencies (shaded region) for the five selected models with  $[M/H] = -0.44$ , and for three different values of the mixing-length parameter  $\alpha = 0.5, 1$ , and  $1.5$ , respectively. For comparison, the predicted growth rates obtained for the model  $A0j$  (with solar metallicity) are also depicted. Although this last model has the same location in the H-R diagram as has its subsolar equivalent model  $0j$ , their physical characteristics (mass, evolutionary stage, etc.) are quite different (see Table 2). This implies differences in their internal structure, which does not necessarily mean that their instability ranges are different. In fact, only the model with  $\alpha_{\text{MLT}} = 0.5$  shows some differences with its equivalent subsolar model. In any case, it can be shown that such differences are not relevant for the present study.

This instability study could be completed by studying the influence of a helium abundance variation due to accretion/diffusion chemical mixing processes. This task will be addressed once the rotationally induced chemical mixing is implemented in our equilibrium models.

#### 4. MULTICOLOR PHOTOMETRY

In the following, multicolor photometry is used to provide constraints on the physical magnitudes of the star and additional information on the degree  $\ell$  of the spherical harmonic associated to each observed pulsational frequency.

The linear approximation to nonradial flux variations of a pulsating star was first derived by Dziembowski (1977), and later reformulated by Balona & Stobie (1979) and Watson (1988). Then, Garrido et al. (1990) showed that “v” and “y” Strömgren bands can be used for discriminating the degree  $\ell$ . The comparison of the numerical solutions with the observations are based on nonadiabatic calculations (more details in Moya 2003; Moya et al. 2004). In particular, pulsation is highly nonadiabatic in stellar surface layers, where thermal relaxation time is either of the same order as, or even lower than, the pulsation period. Accurate determination of the eigenfunctions in these layers, therefore, requires the use of a nonadiabatic description that includes the entire atmosphere. This procedure makes it possible to relate multicolor photometric observables with such eigenfunctions, allowing therefore a direct constraining on some unknown physical parameters through the direct comparison with observations (see Table 3). However, when a star rotates, these multicolor photometric observables may be affected. Therefore we first must evaluate this source of possible confusion.

##### 4.1. Effect of Rotation

For a moderately rotating star, like 29 Cyg, the effects of rotation on the oscillation modes must be taken into account (Dziembowski & Goode 1992; Soufi et al. 1998). In particular, differential rotation and near degeneracy (Suárez et al. 2006) should be considered carefully when searching for detailed asteroseismic models. Note that, according to Suárez et al. (2006), the effect on low-order radial mode frequencies is expected to be much lower than the effect caused by the star deformation due to the centrifugal force. Therefore, for this

**Table 3**  
Observed Amplitudes and Phases (Referred to as  $y$ ) and their Corresponding Error Bars in the Four Bands of the Strömgren System, for the Three Highest Amplitude Frequencies

	$\phi_u - \phi_y$	$\phi_v - \phi_y$	$\phi_b - \phi_y$	$A_u/A_y$	$A_v/A_y$	$A_b/A_y$
$f_1$	$9.5 \pm 5.0$	$-0.9 \pm 3.9$	$0.6 \pm 3.9$	$1.241 \pm 0.112$	$1.345 \pm 0.080$	$1.207 \pm 0.076$
$f_2$	$5.4 \pm 3.6$	$-2.5 \pm 1.7$	$-1.3 \pm 2.7$	$1.195 \pm 0.078$	$1.366 \pm 0.058$	$1.243 \pm 0.055$
$f_3$	$6.9 \pm 1.5$	$-1.6 \pm 1.2$	$-0.6 \pm 1.2$	$1.165 \pm 0.033$	$1.309 \pm 0.024$	$1.186 \pm 0.023$

**Table 4**  
Main Characteristics of the Computed Pseudo-Rotating Models Representative of 29 Cyg with the Two Metallicity Values  $[M/H] = 0.00, -0.44$ , and the Three Rotational Velocities  $\Omega = 80, 94$  and  $120 \text{ km s}^{-1}$ , Respectively<sup>a</sup>

	ID ( $ij$ )	$M/M_\odot$	$\log T_{\text{eff}}$	$\log g$	$\log(L/L_\odot)$	$X_c$	Age	$\nu_f$	$\nu_\Omega$
$\Omega = 80, [Fe/H] = 0.00$	...	...	...	...	...	...	...	...	...
	02	1.84	3.902	4.12	1.14	0.492	642	177.0	9.4
	12	2.09	3.909	3.93	1.42	0.324	690	121.7	7.1
	22	2.01	3.894	3.92	1.35	0.314	785	121.2	7.1
	32	1.76	3.910	4.28	0.99	0.663	154	235.9	11.6
	42	1.68	3.893	4.29	0.90	0.679	105	241.3	12.0
$\Omega = 94, [Fe/H] = 0.00$	...	...	...	...	...	...	...	...	...
	02	1.84	3.902	4.13	1.14	0.499	630	178.2	11.0
	12	2.09	3.909	3.93	1.42	0.331	690	122.5	8.2
	22	2.01	3.894	3.92	1.35	0.319	780	121.5	8.2
	32	1.76	3.910	4.29	0.99	0.678	95	239.4	13.5
	42	1.68	3.893	4.29	0.90	0.682	90	241.0	13.7
$\Omega = 120, [M/H] = 0$	...	...	...	...	...	...	...	...	...
	02	1.84	3.901	4.13	1.13	0.508	603	178.7	14.2
$\Omega = 80, [Fe/H] = -0.44$	...	...	...	...	...	...	...	...	...
	02	1.58	3.902	4.12	1.08	0.367	1250	185.0	10.2
	12	1.81	3.909	3.92	1.36	0.211	1037	127.7	7.5
	22	1.72	3.894	3.93	1.27	0.211	1200	130.8	7.9
	32	1.49	3.910	4.32	0.88	0.595	730	267.2	13.2
	42	1.42	3.892	4.33	0.78	0.622	705	274.6	13.6

**Note.** <sup>a</sup> Label  $i$  from 0 to 4 indicates the location of the models in the H-R diagram given in Figure 1. From left to right,  $\Omega$  represents the rotational velocity in  $\text{km s}^{-1}$ ,  $M$  the stellar mass in solar masses  $M_\odot$ ,  $\log T_{\text{eff}}$  the effective temperature in K (on a logarithmic scale),  $\log g$  the surface gravity in  $\text{cgs}$  (on a logarithmic scale),  $\log(L/L_\odot)$  the luminosity relative to solar luminosity (on a logarithmic scale),  $X_c$  the central hydrogen fraction, the age in Myr;  $\nu_f$  the frequency of the fundamental radial mode (in  $\mu\text{Hz}$ ), and finally,  $\nu_\Omega$  represents the rotational frequency (in  $\mu\text{Hz}$ ) of the model.

particular case, no specific corrections for the effect of differential rotation are required. In the present work we focus on the effect of second-order near degeneracy. As shown by Daszyńska-Daszkiewicz et al. (2002), when modes are degenerate, the rotational coupling affects the amplitude ratios/phase difference diagnostics diagrams. In particular, the loci of different modes in such diagrams become both  $m$  and aspect dependent (i.e., dependent of the visual angle  $i$ ). This is explained by the mixing of the corresponding angular components of the coupled modes, i.e., the so-called mode *contamination* (Suárez et al. 2006, 2007).

Taking all these effects into account, asteroseismic models are built for the five selected models in the photometric error box of 29 Cyg shown in Figure 1, with  $\alpha_{\text{MLT}} = 0.5$ , and the two metallicity values considered. Since there is no available information about the inclination angle of the star,  $i$ , the pseudo-rotating models are computed for three rotational velocities: 80, 94, and  $120 \text{ km s}^{-1}$  (see Table 4). This selection covers a range of reasonable rotational velocities for  $\delta$  Scuti stars. Such a range remains in the limit of validity of the perturbation approach followed in the calculation of the oscillation frequencies. This range of rotational velocities implies a range in  $i$  from  $i = 90^\circ$  to  $i = 41.8^\circ$ , respectively.

The asteroseismic pseudo-rotating models representative of 29 Cyg are then completed by their corresponding oscillation spectra as described in Section 2.3. Due to cancellation effects, only radial and nonradial modes up to  $\ell \leq 3$  are computed. In order to investigate the impact of near degeneracy on mode identification, we select, for each model, the degenerate modes whose frequencies are close to the observed ones. Then, for these degenerate modes, we calculate the so-called contamination coefficients  $\beta_j$  (see Casas et al. 2006 for a similar procedure). We use these contamination coefficients to calculate the amplitude/phase diagrams for modes of Table 5. The aspect dependence is studied varying the angle of inclination  $i$  from  $-180^\circ$  to  $180^\circ$ , by steps of  $\cos i = 0.02$ . In Figure 3, the amplitude ratios/phase difference diagrams are depicted for the  $u$  band (as compared to  $y$ ), for the models with solar abundance (similar results are found for models with  $[M/H] = -0.44$ ). For comparison, the values of the amplitude ratios and phase differences obtained for the nonrotating case are also depicted. Only models with a rotational velocity of  $80 \text{ km s}^{-1}$  are considered, as for the remaining models, similar results are found. This can be explained by the small dependence of the contamination coefficients upon the rotational velocity (see Suárez et al. 2006 for more details). In general, the amplitude

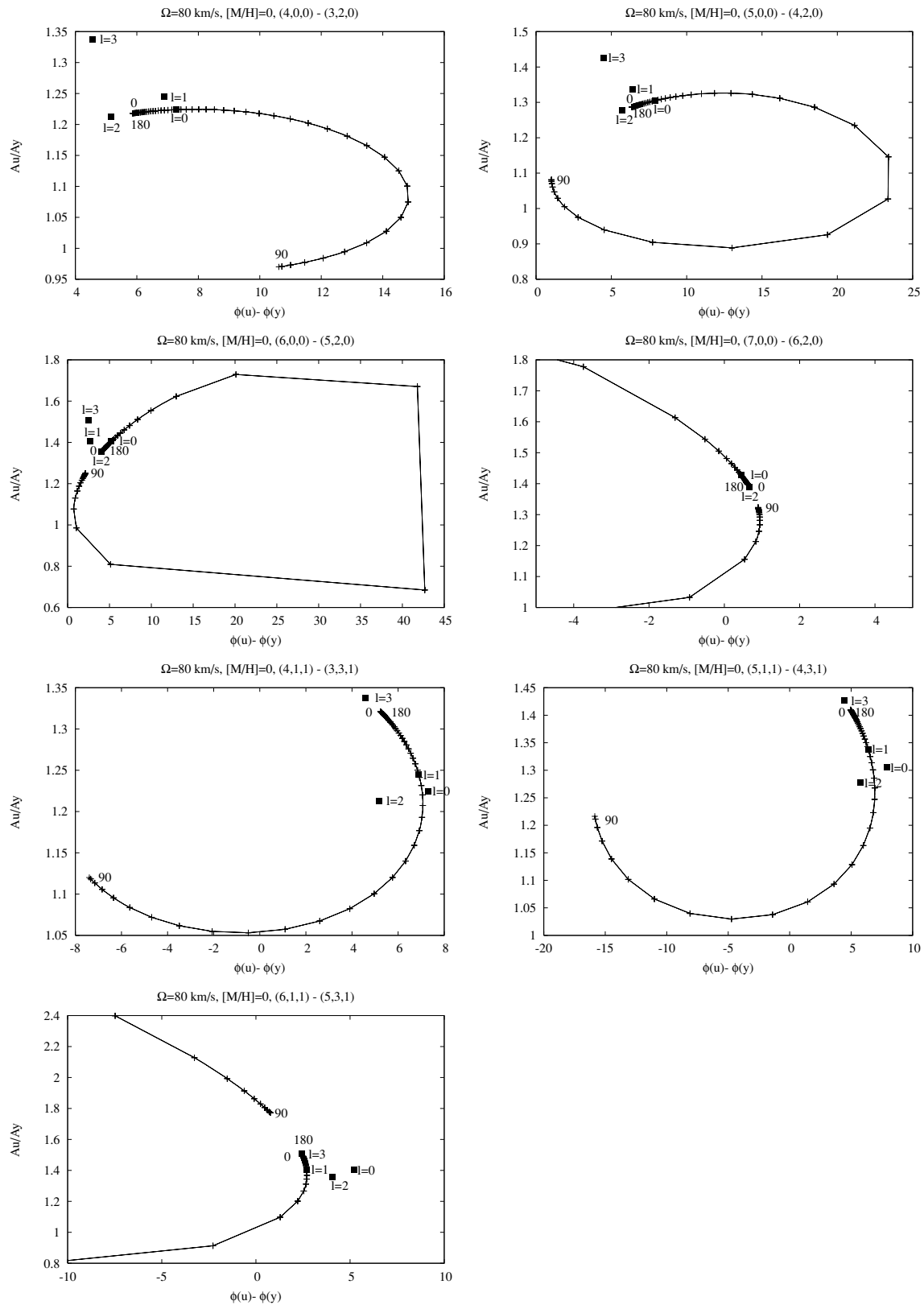


**Figure 3.** Phase–amplitude diagrams for the  $u$  Strömgren band (as compared to  $y$ ), for theoretical near-degenerate modes whose frequencies are close to the observed ones. Only models with solar metallicity are considered. The squares represent the locations of modes obtained when rotation is not taken into account.

and phase predictions seem to concentrate in some regions of the curves, with a high density of points. As expected, this dense region is located between the coupled  $\ell$ , that is, if there are two coupled modes with  $\ell = 0-2$ , most of the angles give

rise to observables in the range limited by the nonrotating  $\ell = 0$  and  $\ell = 2$  values. Similar results are found for the  $\ell = 1-3$  coupling. Besides, this region is clearly different from the rest of the nonrotating  $\ell$  predictions for most of the angles. On the other

**Table 5**  
Coupled Modes Found for the O2 Models with Two Metallicity Values  
[M/H] = 0.00, -0.44, and Three Rotational Velocities  $\Omega = 80, 94,$  and  
120 km s<sup>-1</sup>, Respectively<sup>a</sup>

Model	$n_a, \ell_a, m_a$	$\sigma_a$	$n_b, \ell_b, m_b$	$\sigma_a - \sigma_b$	$\beta_j$
$\Omega = 80, [\text{Fe}/\text{H}] = 0.00$	...	...	...	...	...
	4, 0, 0	333.35	3, 2, 0	2.73	0.15
	<b>4, 1, 1</b>	<b>340.34</b>	<b>3, 3, 1</b>	<b>4.34</b>	<b>0.11</b>
	4, 1, -1	359.04	3, 3, -1	-3.76	0.15
	5, 0, 0	387.00	4, 2, 0	-3.80	0.13
	<b>5, 1, 1</b>	<b>398.61</b>	<b>4, 3, 1</b>	<b>5.07</b>	<b>0.09</b>
	5, 1, -1	417.26	4, 3, -1	-4.61	0.13
$\Omega = 94, [\text{Fe}/\text{H}] = 0.00$	...	...	...	...	...
	4, 0, 0	334.85	3, 2, 0	3.90	0.15
	<b>4, 1, 1</b>	<b>339.72</b>	<b>3, 3, 1</b>	<b>5.90</b>	<b>0.10</b>
	4, 1, -1	361.45	3, 3, -1	-5.22	0.15
	5, 0, 0	388.63	4, 2, 0	-5.41	0.13
	<b>5, 1, 1</b>	<b>398.06</b>	<b>4, 3, 1</b>	<b>6.90</b>	<b>0.09</b>
	5, 1, -1	419.73	4, 3, -1	-6.37	0.13
$\Omega = 120, [\text{Fe}/\text{H}] = 0.00$	...	...	...	...	...
	4, 0, 0	334.18	3, 2, 0	7.29	0.15
	<b>4, 1, 1</b>	<b>333.83</b>	<b>3, 3, 1</b>	<b>10.18</b>	<b>0.11</b>
	5, 0, 0	387.53	4, 2, 0	-9.98	0.13
	<b>5, 1, 1</b>	<b>391.56</b>	<b>4, 3, 1</b>	<b>12.03</b>	<b>0.09</b>
	5, 1, -1	419.69	4, 3, -1	-11.33	0.13
	<b>6, 0, 0</b>	<b>442.69</b>	<b>5, 2, 0</b>	<b>-12.82</b>	<b>0.11</b>
6, 1, 1	448.11	5, 3, 1	14.02	0.08	
$\Omega = 80, [\text{Fe}/\text{H}] = -0.44$	...	...	...	...	...
	<b>5, 0, 0</b>	<b>399.88</b>	<b>4, 2, 0</b>	<b>3.05</b>	<b>0.16</b>
	5, 1, 1	408.85	3, 3, 1	5.86	0.09
	<b>5, 1, -1</b>	<b>429.06</b>	<b>3, 3, -1</b>	<b>5.36</b>	<b>0.06</b>

**Note.** <sup>a</sup> The mode identification is given by its radial order  $n$ , spherical degree  $\ell$ , and azimuthal order  $m$ . The oscillation frequencies are represented by  $\sigma_a$  and  $\sigma_b$  (in  $\mu\text{Hz}$ ). The contamination coefficient is given by  $\beta_j$  (see Casas et al. 2006). Modes corresponding to the observed  $f_1$  (344.63  $\mu\text{Hz}$ ),  $f_2$  (401.74  $\mu\text{Hz}$ ), and  $f_3$  (433.17  $\mu\text{Hz}$ ) are marked in bold face.

hand, the rest of the possible angles, not lying in this region, yield results clearly far from those expected for any nonrotating models.

In summary, if two modes are coupled by rotation, their multicolor photometric observables depend on the inclination angle  $i$ , and two possibilities arise: (1) for most of the angles, the coupled modes give observables between their nonrotating predictions, and (2) there are some angles giving values for these observables far from the nonrotating predictions (see Figure 3). This means that a possible confusion with the rest of the  $\ell$  values in the nonrotating frame is unlikely. Furthermore, some inclination angles can be easily identified, since the multicolor observables are clearly different from the nonrotating predictions. When the  $\ell$ -diagnostic diagrams are performed for the models with  $[\text{Fe}/\text{H}] = -0.44$ , conclusions are similar to those reported for the solar metallicity models. From these diagnostics, no constraints on the  $\lambda$  Bootis nature of the star are obtained. Indeed, the observational uncertainties, especially those of the phase differences, are too large to perform any systematic analysis of the mode identification in presence of near degeneracy. Sufficiently accurate multicolor observations are thus required.

#### 4.2. Amplitude Ratios versus Phase Differences

The computed models described in Section 2.3 provide information not only about the unstable modes, but also about the

nonrotating nonadiabatic quantities necessary to calculate phase differences and amplitude ratios for the different Strömgen colors. Theoretical predictions of both quantities are then compared with the observed ones for  $f_1, f_2,$  and  $f_3$ . We do not extend the study to the rest of the observed frequencies due to their large error bars, rendering that extension of the study meaningless. For the sake of clarity and brevity, diagnostic diagrams are depicted only for the  $Ai2$  sets of models (i.e., those with  $\alpha_{\text{MLT}} = 0.5$ ) without rotation and solar metallicity. The selected reference band for amplitude ratios and phase differences is band  $y$ .

For each  $Aij$  model, the theoretical frequencies used to build these diagrams are the closest to the observed ones, within an uncertainty of  $\approx 5\%$  (in frequency), which includes effects coming from rotation,  $\alpha$ , and metallicity observational errors. A detailed analysis reveals that the uncertainty coming from rotation largely dominates.

Let us examine the results for the different models, combining information from Figures 3–8, and Table 5.

*A0j* models (Figure 4):

1. For  $f_1$ , the nonrotating predictions agree with the observations. A possible coupling of  $\ell = 1-3$  modes is found in Table 5. In this case, inclination angles are constrained to those not changing the color index significantly. Therefore,  $f_1$  can be identified as  $\ell = 0$  or a coupling of  $\ell = 1-3$ .
2. The mode  $f_2$  may be interpreted as a coupling of  $\ell = 1-3$  modes. As the nonrotating predictions give an amplitude ratio between the  $u$  and  $y$  bands larger than observations, the only possible interpretation is that the observed mode suffers a rotational coupling, with a visual angle  $i = [70, 75]$  deg. Nevertheless, a noncoupled  $\ell = 0$  or 2 mode cannot be completely discarded since the theoretical predictions are close to the limit of the observational errors.
3. An important consequence of this analysis is that  $f_3$  cannot be correctly identified for any  $\alpha_{\text{MLT}}$ . No coupling is predicted for this frequency, and the observed values for the  $u$  band do not fit any of the nonrotating predictions.

*A1j* models (Figure 5): for the following mode identifications, we use the same procedure showed in the  $A0j$  case. As  $\alpha_{\text{MLT}}$  decreases,  $f_1$  and  $f_2$  theoretical predictions are closer to observations. However, for  $f_1$  the amplitude ratios between the  $u$  and  $y$  bands cannot be reproduced, since no coupling is predicted for this mode. For  $f_2$ , the amplitude ratios for all bands cannot be reproduced in any case. This also occurs for  $f_3$  and the observations with the  $u$  band.

*A2j* models (Figure 6): in the case of  $f_1$ , the only possible identification compatible with the  $u$  band is a coupling of  $\ell = 0-2$  modes, but for a small range of  $i$  angles. This possibility, pointed out by Daszyńska-Daszkiewicz et al. (2002), thus, becomes very unlikely. The  $u$  band for  $f_2$  and  $f_3$  cannot be reproduced in any of the scenarios considered here. This behavior is not necessarily inconsistent with the finding that the phase differences with the  $v$  band of both frequencies are not predicted.

*A3j* models (Figure 7): only one mode has a frequency close to the observed  $f_1$ . For this mode, the multicolor observables fit the observations except for the phase differences in the  $u$  band. Note that these results are close to the upper limit, therefore this identification cannot be completely discarded. The mode  $f_2$  can only be interpreted as a dipole mode. Finally, the nonadiabatic observables for the  $u$  band of  $f_3$  can only be fitted if the observed mode is a coupling of  $\ell = 0-2$  modes, for a small  $i$  range. Nevertheless, the amplitude ratio for the  $v$  band cannot be

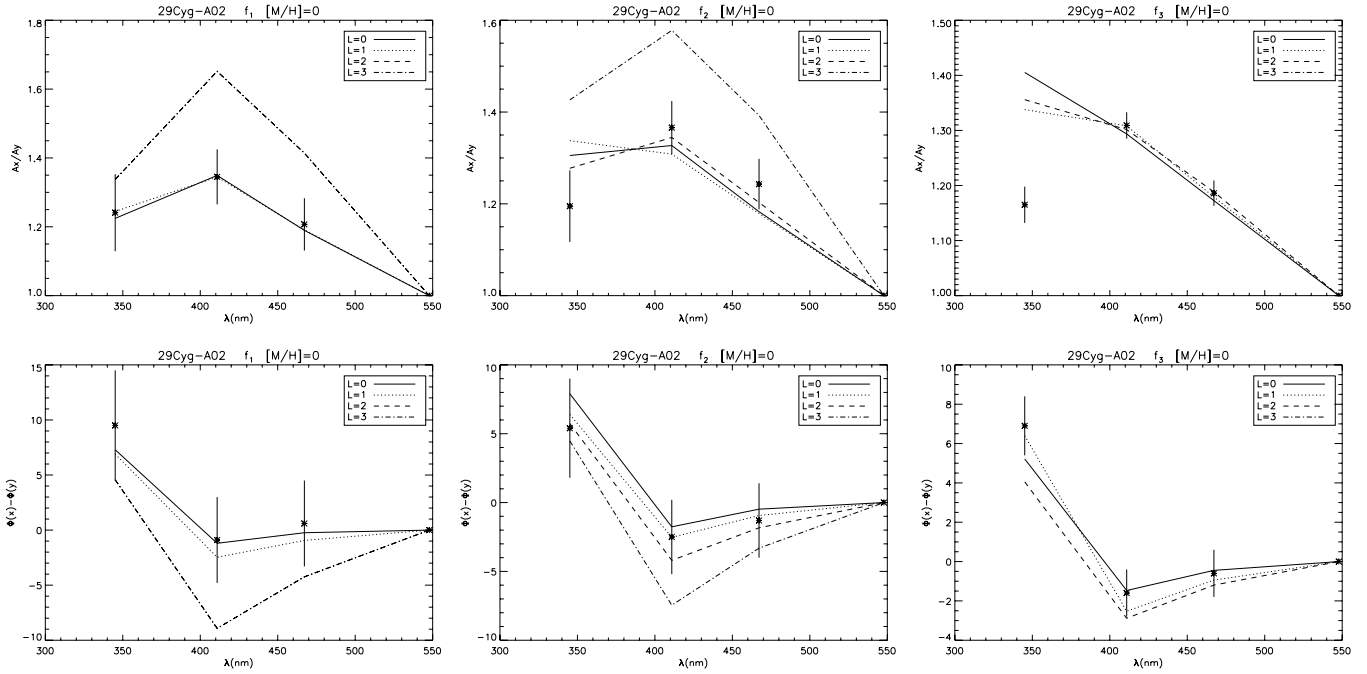


**Figure 4.** Amplitude ratios (top row) and phase differences (bottom row) for models A02 ( $\alpha_{MLT} = 0.5$  and  $[M/H] = 0$ ), calculated for the observational frequencies  $f_1$  (left column),  $f_2$  (center column), and  $f_3$  (right column), respectively. Observed Strömgren bands are represented by asterisks.

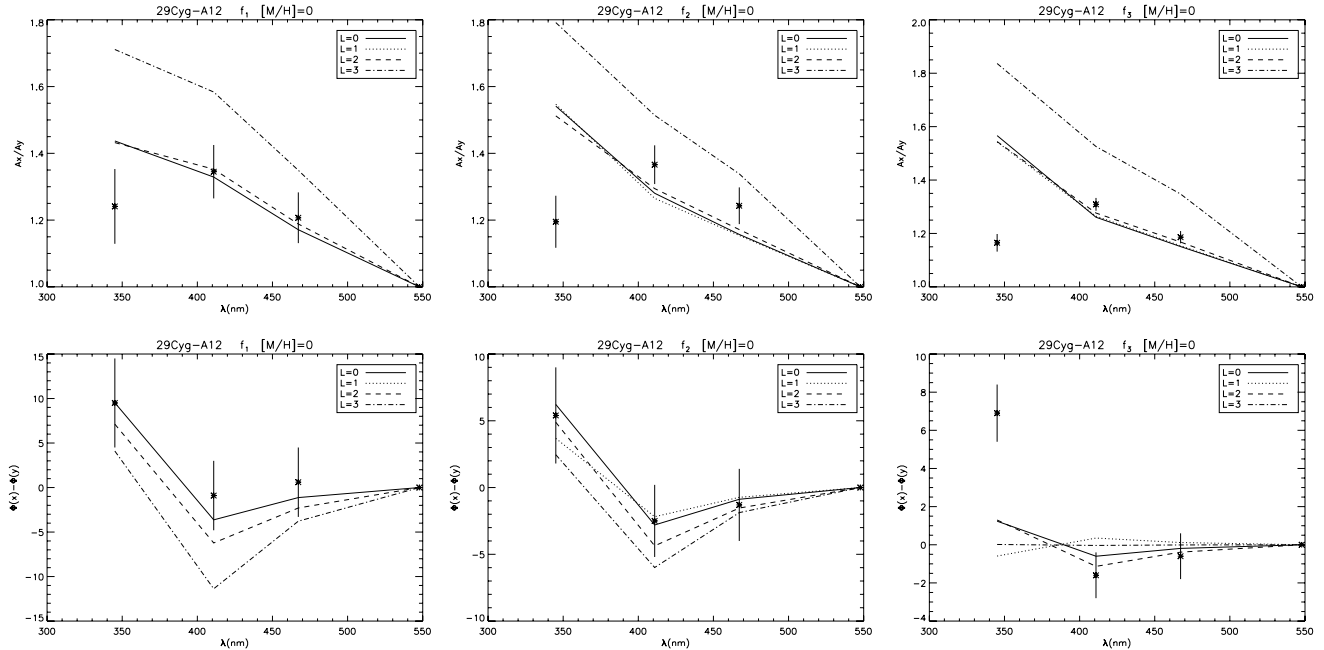


**Figure 5.** Amplitude ratios (top row) and phase differences (bottom row) for models A12 ( $\alpha_{MLT} = 0.5$  and  $[M/H] = 0$ ), calculated for the observational frequencies  $f_1$  (left column),  $f_2$  (center column), and  $f_3$  (right column), respectively. Observed Strömgren bands are represented by asterisks.

reproduced. These two conditions make this identification very unlikely.

*A4j models* (Figure 8): these models give a mode identification similar to *A3j*, except that, in this case, a radial mode can also be associated to  $f_2$ , and  $f_1$  is now identified as  $\ell = 1$ .

This study was also carried out for models with subsolar metallicity ( $[M/H] = -0.44$ ), and the main results are summarized as follows:

1. *0j* models: the  $f_1$  mode can be interpreted as  $\ell = 0$  or 2, frequency  $f_2$  as  $\ell = 2$  or a coupling of  $\ell = 0-2$ , and  $f_3$  can

only be a  $\ell = 1-3$  coupled mode, in a range of inclination angle  $i = [70, 75]$  deg.

2. *1j* and *2j* models: all modes have to be interpreted as coupled modes, but the inclination angles required to fit each frequency are not coherent. Therefore, these models are unable to reproduce the observations.
3. *3j* and *4j* models: these models provide a reasonable fitting of the observations, except the amplitude ratio in the band  $\nu$  for  $f_3$ . The *4j* models match the results better than the *3j* models.

Therefore, although both groups of models (with solar and subsolar metallicity) yield similar results, the subsolar ones

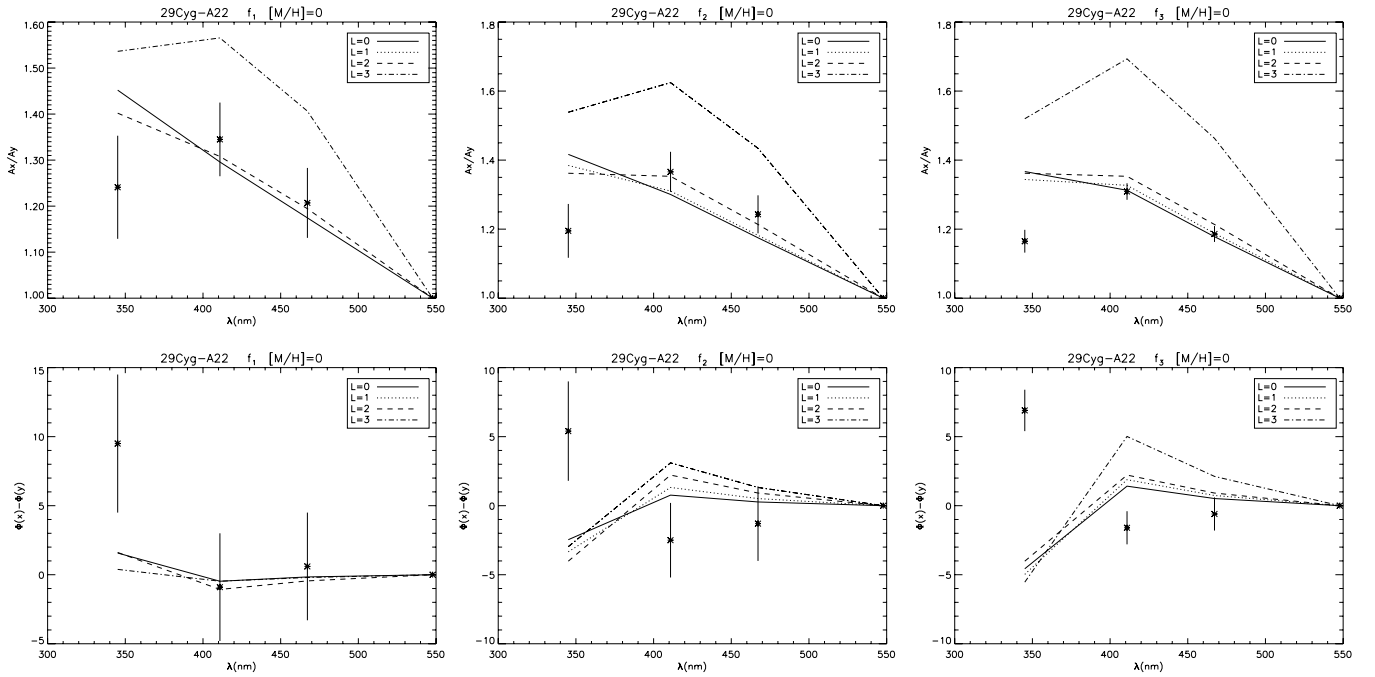


**Figure 6.** Amplitude ratios (top row) and phase differences (bottom row) for models A22 ( $\alpha_{\text{MLT}} = 0.5$  and  $[M/H] = 0$ ), calculated for the observational frequencies  $f_1$  (left column),  $f_2$  (center column), and  $f_3$  (right column), respectively. Observed Strömgren bands are represented by asterisks.

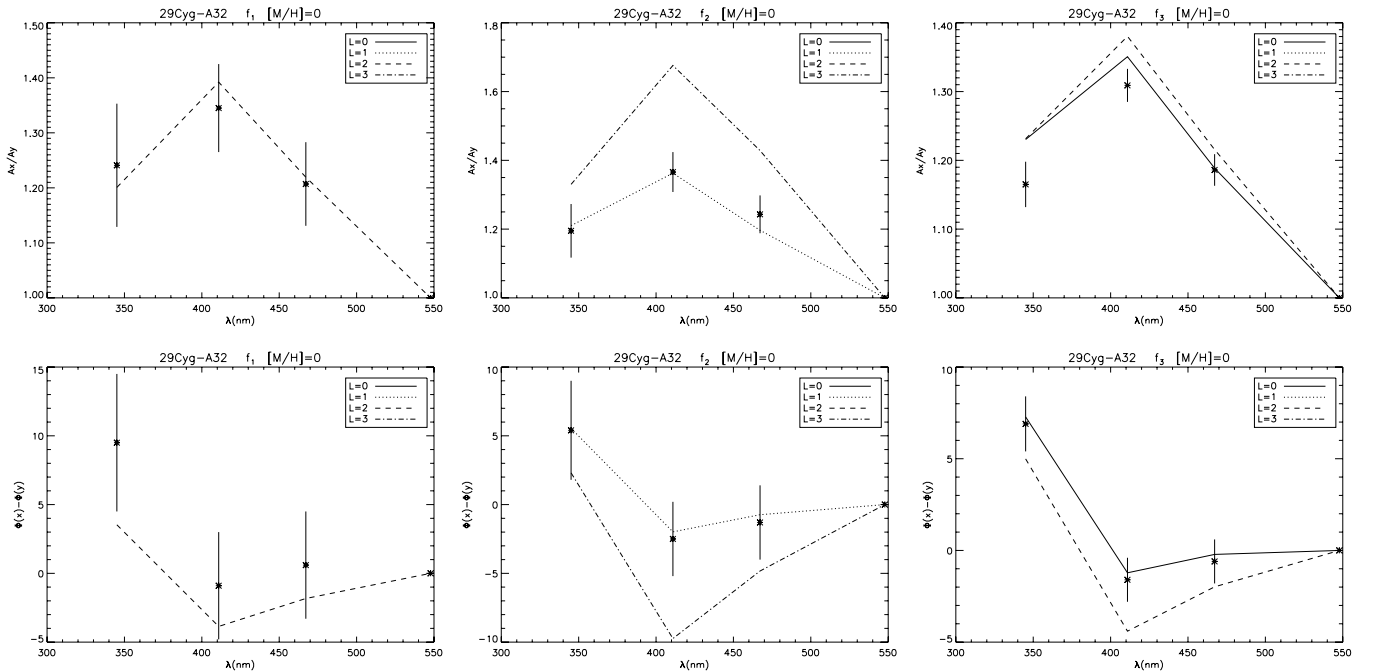


**Figure 7.** Amplitude ratios (top row) and phase differences (bottom row) for models A32 ( $\alpha_{\text{MLT}} = 0.5$  and  $[M/H] = 0$ ), calculated for the observational frequencies  $f_1$  (left column),  $f_2$  (center column), and  $f_3$  (right column), respectively. Observed Strömgren bands are represented by asterisks.

fit the observations better. Note that this study shows better agreement for models in the bottom part of the H-R uncertainty box. In the center of the H-R uncertainty box, only models with subsolar metallicity fit the observations, since  $f_3$  is predicted to be coupled by rotation, fitting observations for the  $u$  band. The mode identification of  $f_3$  with solar metallicity models is very unlikely. A summary of the possible mode identifications for all the studied models can be found in Table 6.

The identification for  $f_3$  is not coincident with that given in Mkrtychian et al. (2007) ( $\ell = 2, n = 5$ ). Unfortunately, in that work there is not a detailed explanation of the characteristics of

the model used. Therefore, the origin of this discrepancy cannot be checked.

Once this analysis has offered some possible mode identifications and some models fulfilling better all the constraints, the fitting of the rest of the frequencies displayed in Table 1 has been verified. Unfortunately, 14 frequencies are not enough to find any spacing pattern and, taking into account modes up to  $\ell = 3$ , and splitted by rotation, we can always find a theoretical mode close to any observed one. Therefore, the direct frequency comparison is not meaningful with the present observational data.

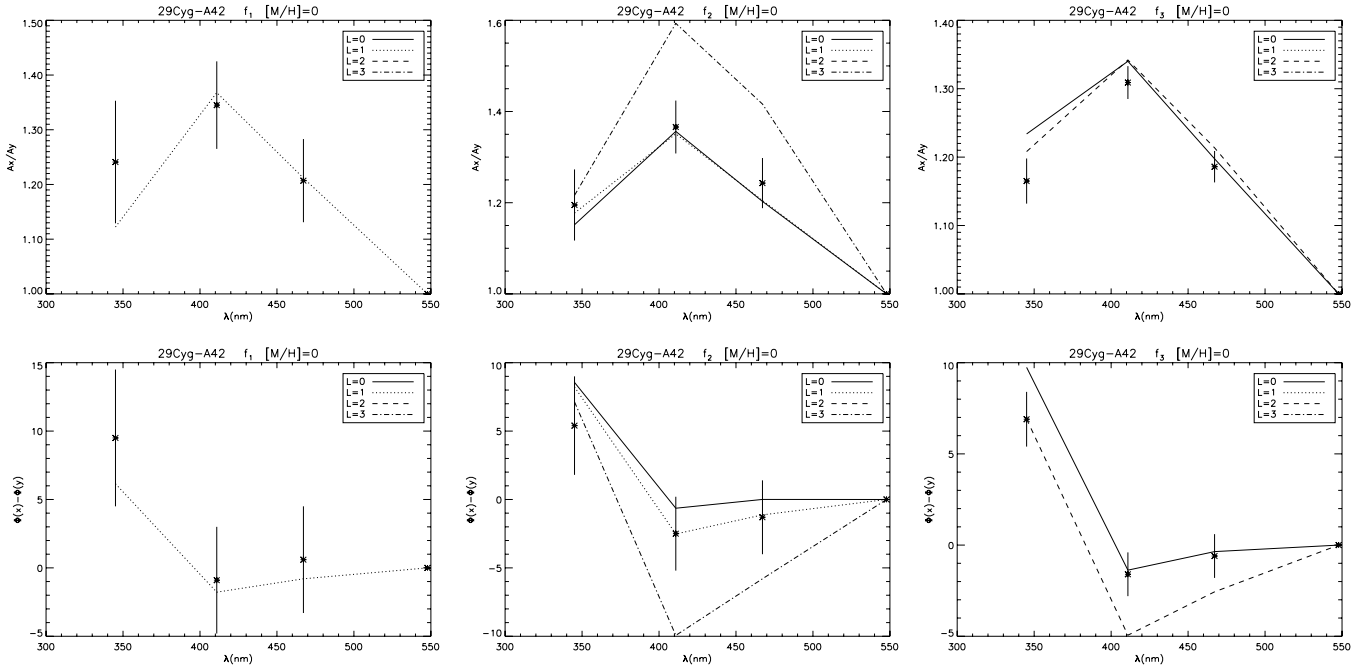


**Figure 8.** Amplitude ratios (top row) and phase differences (bottom row) for models A42 ( $\alpha_{MLT} = 0.5$  and  $[M/H] = 0$ ), calculated for the observational frequencies  $f_1$  (left column),  $f_2$  (center column), and  $f_3$  (right column), respectively. Observed Strömgen bands are represented by asterisks.

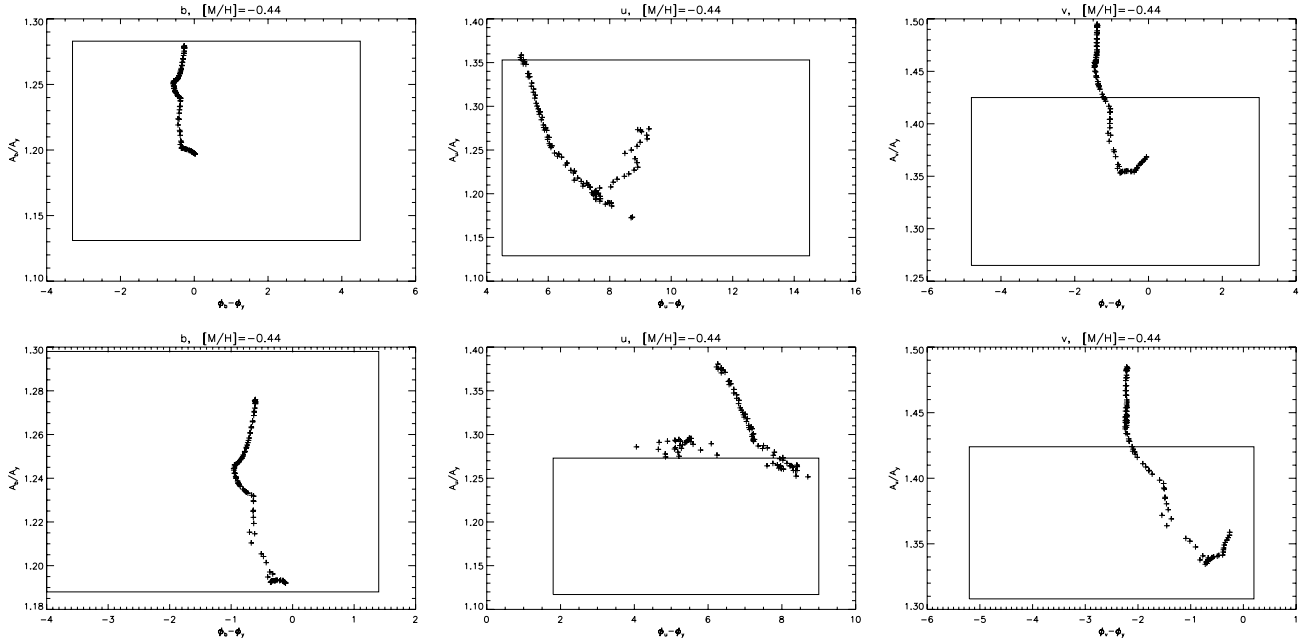


**Figure 9.** Phase–amplitude diagrams showing the evolution of the  $f_1$  (top panels) and  $f_2$  (bottom panels) for the model 02 with subsolar metallicity. From left to right, the different panels depict the results for the Strömgen bands  $b$ ,  $u$ , and  $v$ , using the  $y$  band as reference, respectively.

5. COMPLEMENTARY TECHNIQUES

To obtain additional constraints, two complementary techniques are developed. These techniques are very dependent on the observational data uncertainties and on the previous mode identification. Nevertheless, they can be useful for future studies.

5.1. Evolution of Color Indices

The evolution of the color indices along the evolutionary track, with  $\alpha_{MLT} = 0.5$  and subsolar metallicity (02 models),

passing by the center of the photometric error box of this star, for the frequencies  $f_1$  and  $f_2$ , have been studied. To do so, the three bands  $u$ ,  $v$ , and  $b$  have been included in this study. We have used the mode identification of these two modes best fitting the observations, i.e., ( $n = 4, \ell = 0$ ) and the ( $n = 5, \ell = 0$ ) part of the corresponding coupled mode, respectively (see Figure 9).

During the main part of the stellar evolution, models present color indices in good agreement with observations, taking into account the large error box. Keeping only the models both lying inside the photometric error box and with the identified modes having a frequency  $\pm 5\%$  around the observed  $f_1$  and  $f_2$ , it is

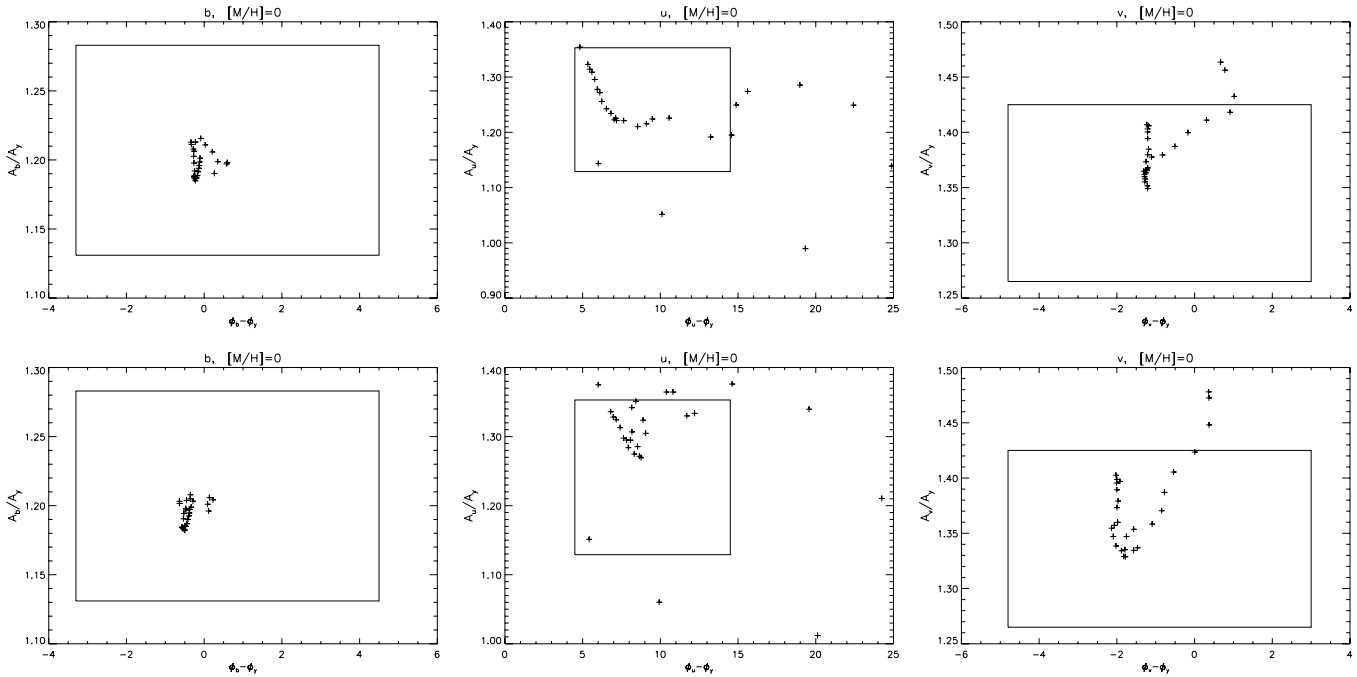


**Figure 10.** Phase–amplitude diagrams showing the evolution of the  $f_1$  (top panels) and  $f_2$  (bottom panels) for the model A02 with solar metallicity. From left to right, the different panels depict the results for the Strömgren bands  $b$ ,  $u$ , and  $v$ , using the  $y$  band as reference, respectively.

**Table 6**

Possible Mode Identification ( $n, \ell$ ) for  $f_1, f_2$ , and  $f_3$  Obtained with Multicolor Photometry<sup>a</sup>

ID	$f_1$	$f_2$	$f_3$
02	(4,0) (2,2)	(3,2) [(5,0)-(4,2)]	[(5,1)-(3,3)]
12	...	...	...
22	...	...	...
32	(2,0) (2,1)	(3,0) (2,2)	(3,0) (3,1)
42	(2,0) (2,1) (1,2)	(3,0) (2,2)	(3,0) (3,1)
A02	(4,0) [(4,1)-(3,3)]	(5,0) (5,2) [(5,1)-(4,3)]	...
A12	...	...	...
A22	...	...	...
A32	(2,2)	(3,1)	[(4,0)-(3,2)]
A42	(2,1)	(3,0) (3,1)	[(4,0)-(3,2)]

**Note.** <sup>a</sup> Coupled modes are within square brackets.

possible to constrain the range of fundamental parameters given by observations. The left and right panels of Figure 9 indicate that both oscillation frequencies provide similar constraints on the age and the effective temperature of the models. Note that the  $u$  filter values for  $f_2$  and subsolar metallicity give values mainly larger than observed. The reason is that this is a coupled mode, and can be affected by the value of  $i$ . Therefore this panel cannot be used for the present discrimination. Using the rest of the panels, the effective temperature and evolutionary stage are constrained to [7870, 8035] K and [1250, 1360] Myr, respectively. These ranges are unusually narrow when compared with typical asteroseismic modeling of  $\delta$  Scuti stars. For models with solar metallicity, this study provides an effective temperature and evolutionary stage of [7943, 8072] K and [600, 700] Myr, respectively (see Figure 10).

In this procedure, the oscillation frequency gives the largest constraint for the temperature and age determination. Nevertheless, the large uncertainties associated with the photometric observations compromise the efficiency of the method. Therefore, with more accurate observations we could better constrain

the temperature and age of the star and, if any of the modes is a coupled mode, we can have an estimate of the inclination angle,  $i$ .

## 5.2. Generalized Petersen Diagrams

The presence of possible radial modes in the observed oscillation spectra of the star may provide additional information. In fact, the effect of rotation on mode frequencies is systematic and less significant for radial modes than for nonradial modes. Therefore, it is plausible to compare ratios of observed radial modes with those predicted by the theory. We illustrate this with the  $i2$  and  $Ai2$  models. In Figure 11, we compare the observed fourth-to-third radial overtones period ratio ( $f_1/f_2$ , Table 1) with the theoretical predictions obtained for representative models with solar and subsolar ( $[Fe/H] = -0.44$ ) metallicity, respectively. For the five models considered in each metallicity case, the corresponding period ratios  $\Pi_{4/3}$  for solar-metallicity tracks are systematically closer to the observations than the subsolar-metallicity tracks. However, they are not yet within the range of the observations. This means that  $f_1$  and  $f_2$  cannot be radial modes at the same time, constraining the possible modal identifications.

On the other hand, we have also studied the possible radial modes identified with the  $3j$  and  $4j$  models for the  $f_1$  and  $f_2$  frequencies, and the discrepancies with observations are even larger.

Note that the present results could be different when accounting for several physical phenomena which can modify the period ratios, including rotation. Cox et al. (1984) proposed that He gradients due to diffusion (during evolution) in the stellar envelopes are responsible for the increase of the period ratios (regardless of the increase due to evolution). On the other hand, Guzik & Cox (1991) point out that the aforementioned period-ratio additional increase cannot be theoretically explained by helium diffusion, because the evolution timescale through the  $\delta$  Scuti instability strip is of the order of  $10^7$  years, which is much shorter than the

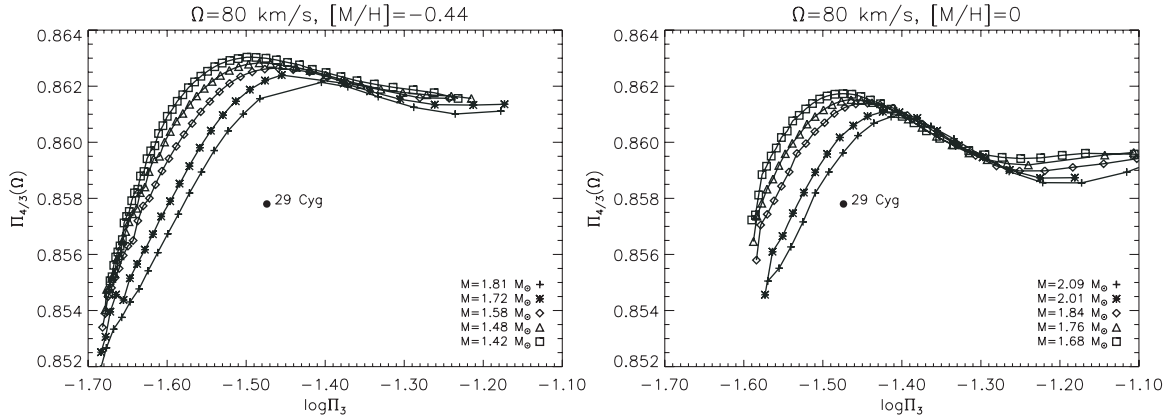


**Figure 11.** Fourth-to-third radial overtones period ratio  $\Pi_4/\Pi_3$  evolution as a function of the  $\Pi_3$  period (in d), for the evolutionary sequences of  $i2$  models with a rotational velocity of  $80 \text{ km s}^{-1}$  (see Table 4) for models with solar (left panel) and subsolar  $[Fe/H] = -0.44$  (right panel) metallic contents. The filled symbol represents the observed  $f_1/f_2$  (see Table 1) for  $\delta$  Scuti star 29 Cyg.

diffusion timescale ( $10^8$  years). In addition, complete surface helium depletion would produce a maximum period decrease of only about 15% of the period increase expected from evolutionary changes. In any case, the additional period ratio expected for  $\delta$  Scuti type stars is about 0.01 maximum. This is clearly much smaller than the difference between the observed and theoretical period ratios found in the present work (see, for instance Figure 11). In addition, the aforementioned effects are of the same order (or even lower) than the effects of rotation on period ratios found by Suárez et al. (2006) and Suárez et al. (2007).

## 6. CONCLUSIONS

The star 29 Cygni has been studied in order to provide some information on its  $\lambda$  Bootis phenomenon. A first thorough asteroseismological analysis has been carried out for this type of star with the help of the most recent multicolor photometric observations and some of the most complete computational tools. The main results are summarized as follows: (1) representative models of the star predict all the observed modes to be unstable, (2) the only models providing a mode identification for  $f_3$  are  $0j$ ,  $3j$ ,  $4j$ ,  $A3j$ , and  $A4j$ ; except for  $3j$  and  $4j$ , this identification is possible only if this observed mode is interpreted as a rotational coupling of two modes, (3) the  $f_1$  and  $f_2$  modes cannot be radial modes at the same time, and (4) for those subsolar metallicity models proving a possible mode identification for the three frequencies, the determined age of the star is in the range [770, 1200] Myr, and its mass between 1.42 and  $1.57 M_\odot$ . This range of ages covers the age given by Paunzen et al. (2002) for this star. The range of masses is not the same. Similarly, in the case of models with solar metallicity the results are [100, 170] Myr for the age, and  $[1.67, 1.75]M_\odot$  for the mass, far from the Paunzen et al. (2002) results. Nevertheless, it must be taken into account that the mode identification provided by these solar metallicity models for  $f_3$  is very unlikely.

Hence, two main conclusions can here be reported.

1. This study is not conclusive regarding the metallicity of this star. On the one hand, the models with solar metallicity which better fit the observations are the youngest ones, but their mode identifications are very unlikely. Nevertheless, the particular case of a model at the center of the photometric error box, with solar metallicity, a large rotational velocity (larger than  $100 \text{ km s}^{-1}$ ) and a certain inclination angle,  $i$ , around  $70$  deg, would be the model

which best fits the observations. On the other hand, the models with subsolar metallicity are the set of models which most likely fit the observations, especially  $3j$  and  $4j$  models, at the bottom of the photometric error box.

2. This star seems to be in the middle of the main sequence. This result is not compatible with the hypothesis of the  $\lambda$  Bootis phenomenon which places the star on the ZAMS or pre-MS, and still connected to its primordial cloud of gas and dust (see Paunzen et al. 2002).

Therefore, the present study suggests the explanation for the nature of the  $\lambda$  Bootis stars as submetallic Pop. I objects affected by chemical transport phenomena (such as rotationally induced mixing, radiative levitation, etc.) or crossing a gas cloud. Nevertheless, the procedure presented here would require more accurate observational data in order to be more conclusive.

This work was partially financed by the Spanish Plan Nacional del Espacio, under project ESP2004-03855-C03-01, and by the Spanish Plan Nacional de Astronomía y Astrofísica, under project AYA2003-04651. We also thank the anonymous referee for useful comments and corrections that helped us to improve this manuscript. J.C.S. acknowledges support by the Instituto de Astrofísica de Andalucía by an I3P contract financed by the European Social Fund and from the Spanish Plan Nacional del Espacio under project ESP2007-65480-C02-01. P. J. A. acknowledges financial support from a “Ramón y Cajal” contract of the Spanish Ministry of Education and Science. A. M. acknowledges financial support from a “Juan de la Cierva” contract of the Spanish Ministry of Education and Science.

## REFERENCES

- Alexander, D. R., & Ferguson, J. W. 1994, *ApJ*, 437, 879  
Balona, L. A., & Stobie, R. S. 1979, *MNRAS*, 189, 649  
Casas, R., Suárez, J. C., Moya, A., & Garrido, R. 2006, *A&A*, 455, 1019  
Charbonneau, P. 1993, *ApJ*, 405, 720  
Christensen-Dalsgaard, J., & Daeppen, W. 1992, *A&AR*, 4, 267  
Cox, A. N., McNamara, B. J., & Ryan, W. 1984, *ApJ*, 284, 250  
Daszyńska-Daszkiewicz, J., Dziembowski, W. A., Pamyatnykh, A. A., & Goupil, M.-J. 2002, *A&A*, 392, 151  
Dupret, M.-A., De Ridder, J., Neuforge, C., Aerts, C., & Scuflaire, R. 2002, *A&A*, 385, 563  
Dziembowski, W. 1977, *Acta Astron.*, 27, 203  
Dziembowski, W. A., & Goode, P. R. 1992, *ApJ*, 394, 670  
Garrido, R., Garcia-Lobo, E., & Rodriguez, E. 1990, *A&A*, 234, 262  
Gies, D. R., & Percy, J. R. 1977, *AJ*, 82, 166  
Gray, R. O., & Corbally, C. J. 2002, *AJ*, 124, 989

- Grevesse, N., & Noels, A. 1993, in *Origin and Evolution of the Elements*, ed. N. Prantzos, E. Vangioni, & M. Cassé (Cambridge: Cambridge Univ. Press), 14
- Guzik, J. A., & Cox, A. N. 1991, *Delta Scuti Star Newsl.*, 3, 6
- Handler, G., & Paunzen, E. 1995, *Delta Scuti Star Newsl.*, 9, 6
- Heiter, U., Weiss, W. W., & Paunzen, E. 2002, *A&A*, 381, 971
- Iglesias, C. A., & Rogers, F. J. 1996, *ApJ*, 464, 943
- Kamp, I., & Paunzen, E. 2002, *MNRAS*, 335, L45
- Kusakin, A. V., & Mkrichian, D. E. 1996, *Inf. Bull. Var. Stars*, 4314, 1
- Michaud, G., & Charland, Y. 1986, *ApJ*, 311, 326
- Michel, E., et al. 1999, *A&A*, 342, 153
- Mkrichian, D. E., et al. 2007, *AJ*, 134, 1713
- Morel, P. 1997, *A&AS*, 124, 597
- Morgan, W. W., Keenan, P. C., & Kellman, E. 1943, *An Atlas of Stellar Spectra, with an Outline of Spectral Classification* (Chicago, IL: Univ. Chicago Press)
- Moya, A. 2003, PhD thesis, Univ. Granada
- Moya, A., Garrido, R., & Dupret, M. A. 2004, *A&A*, 414, 1081
- Paunzen, E. 1998, *Contrib. Astron. Obs. Skalnaté Pleso*, 27, 395
- Paunzen, E. 2003, *Recent Res. Devel. Astron. Astrophys.*, 1, 1
- Paunzen, E., & Handler, G. 1996, *Inf. Bull. Var. Stars*, 4318, 1
- Paunzen, E., Iliev, I. K., Kamp, I., & Barzova, I. S. 2002, *MNRAS*, 336, 1030
- Pérez Hernández, F., Claret, A., Hernández, M. M., & Michel, E. 1999, *A&A*, 346, 586
- Rodríguez, E., López-González, M. J., & López de Coca, P. 2000, *A&AS*, 144, 469
- Rolland, A., Hobart, M. A., Costa, V., Rodríguez, E., Olivares, I., López de Coca, P., & García-Pelayo, J. M. 2002, in *Stellar Structure and Habitable Planet Finding*, ed. F. Favata, I. W. Roxburgh, & D. Galadi (ESA SP-485; Noordwijk: ESA), 333
- Soufi, F., Goupil, M. J., & Dziembowski, W. A. 1998, *A&A*, 334, 911
- Suárez, J. C. 2002, PhD thesis, Univ Paris
- Suárez, J. C., Garrido, R., & Goupil, M. J. 2006, *A&A*, 447, 649
- Suárez, J. C., Garrido, R., & Moya, A. 2007, *A&A*, 474, 961
- Suárez, J. C., Goupil, M. J., & Morel, P. 2006, *A&A*, 449, 673
- Suárez, J.-C., Michel, E., Pérez Hernández, F., Lebreton, Y., Li, Z. P., & Fox Machado, L. 2002, *A&A*, 390, 523
- Tran Minh, F., & Léon, L. 1995, in *Physical Processes in Astrophysics*, ed. I. W. Roxburgh & J. L. Maxnou (Berlin: Springer), 219
- Turcotte, S., & Charbonneau, P. 1993, *ApJ*, 413, 376
- Venn, K. A., & Lambert, D. L. 1990, *ApJ*, 363, 234
- Watson, R. D. 1988, *Ap&SS*, 140, 255
- Winzer, J. E. 1974, PhD thesis, Univ. Toronto
- Zahn, J.-P. 1992, *A&A*, 265, 115